Journal of Alloys and Compounds 956 (2023) 170310

Contents lists available at ScienceDirect

Journal of Alloys and Compounds

journal homepage: www.elsevier.com/locate/jalcom

Research Article

Thermomechanical treatments for a dual phase cast high entropy alloy

Ricardo Henrique Buzolin [a,b,*], Markus Masswohl [a,b], Franz Miller Branco Ferraz [a,b], Konrad Chrzan [c], Tomasz Dudziak [c], Maria Cecilia Poletti [a,b]

[a] Christian Doppler Laboratory for Design of High-Performance Alloys by Thermomechanical Processing, Kopernikusgasse 24, 8010 Graz, Austria
[b] Institute of Materials Science, Joining and Forming at Graz University of Technology, Kopernikusgasse 24/I, 8010 Graz, Austria
[c] Sieć Badawcza Łukasiewicz - Krakowski Instytut Technologiczny, ul. Zakopiańska 73, 30-418 Kraków, Poland

ARTICLE INFO

Article history:
Received 5 January 2023
Received in revised form 23 April 2023
Accepted 25 April 2023
Available online 26 April 2023

Keywords:
High entropy alloys
Hot deformation
Annealing
Recrystallisation
Recovery
Microstructure design

ABSTRACT

Thermomechanical treatments modify the cast microstructure of a dual phase hypoeutectic high entropy alloy. The as-cast microstructure consists of an FCC matrix and a BCC eutectic phase forming a semi-continuous network. The as-cast material is subjected to various thermomechanical treatments: I) hot compression; II) hot compression with strain rate jumps; III) multi-stage hot compression with intermediate stages of isothermal soaking; IV) hot compression followed by annealing. The material recovers rapidly after the strain rate jump and no dependence of the yield stress on the previous deformation step is observed. Much of the stress relaxation occurs within seconds during the hold for the multi-stage tests. A steady-state stress is reached for the first holding cycle, while progressively slower softening is observed for later holding cycles. The eutectic BCC phase fragments during hot deformation, while discontinuous dynamic recrystallisation associated with the formation of Σ3 occurs in the FCC phase. Precipitates are formed at high temperatures and pin the high-angle grain boundary motion. The rotation of the eutectic BCC phase and the precipitates during plastic deformation also promotes local lattice rotation of the FCC phase. As a result, a fine and intricate substructure is formed in the interdendritic spaces. Complete recrystallisation is not achieved during either hot deformation or annealing, suggesting that practical grain refinement of the investigated alloy would only be achieved at larger strains or a combination of larger deformations and intermediate annealing treatments.

1. Introduction

Multi-principal element alloys, also known as medium entropy alloys (MEAs) or high entropy alloys (HEAs), are part of a class of materials that has been developed in recent years [1–4]. HEAs are metallic alloys with four or more main elements, each with concentrations between 5 and 35 at% [5,6]. The classification of the HEAs is based on their chemical composition [7] or their strengthening mechanisms [2]. The face-centred cubic (FCC) based HEAs exhibit a high strength/ductility combination [8], impact toughness [9], high-temperature corrosion and oxidation resistance, and wear resistance [10–13]. The FCC phase in the HEAs is typically a low stacking fault energy phase [14–16]. However, the SFE of the FCC phase increases with temperature [17], which reduces the stability of stacking faults [18]. Al additions can further improve the combined effects of high configurational entropy, severe lattice distortion and the "cocktail" effect [5], typical of FCC-based HEAs [19–21]. Al has a strong, cohesive bond with the other elements present in typical FCC-based HEAs, providing additional solid-solution strengthening [22]. Al also provokes the formation of a hard body-centred cubic (BCC) phase (ordered (B_2) + disordered (A_2)) for Al atomic fraction higher than 0.45 [23]. The $L1_2$ ordered phase can also be formed [24], as well as the $L2_1$ phase if Ti is added [25]. Annealing can form a stable duplex structure is formed from the metastable ordered B2, and disordered A2 phases [26]. In the as-cast state, finely dispersed BCC particles are distributed in an FCC matrix at low Al additions. At high Al contents, allotriomorphic and intragranular FCC particles can be formed in a BCC matrix [26]. The FCC-based HEAs with Al exhibit similar behaviour to Ni-base superalloys containing FCC and BCC phases. The strengthening of the BCC phase due to thermally activated cross-slip of dislocations from the octahedral {111} to the cube {100} within the BCC phase [27] leads to an abnormal increase in strength with increase in temperature [28]. The high ductility and formability of the FCC phase can be combined with the high strength of the BCC phase in the duplex structure obtained in the Al-containing FCC-based HEAs [29].

* Corresponding authour at: Christian Doppler Laboratory for Design of High-Performance Alloys by Thermomechanical Processing, Kopernikusgasse 24, 8010 Graz, Austria.
E-mail address: ricardo.buzolin@tugraz.at (R.H. Buzolin).

https://doi.org/10.1016/j.jallcom.2023.170310

Among the dual-phase HEA, the eutectic HEA have excellent castability since the mushy zone (lack of solidification range) and micro-segregation, can be avoided. Since the eutectic reaction is an isothermal transformation, there is no solidification temperature range, minimising both the segregation and shrinkage cavity [30]. The eutectic HEA are formed by a soft FCC phase and a hard BCC phase, providing acceptable combination of strength and ductility and excellent work hardening capacity [31,32]. Lu et al. [30] developed the first eutectic HEA with the composition of $AlCoCrFeNi_{2.1}$. It consists of a lamellar micro-structure including B_2 ordered phases and had outstanding mechanical stability up to 700 °C. Asoushe et al. [33] also investigated the thermal phase-stability of the same chemical composition and found that the volume fractions of FCC and BCC phases did not notably change up to 500 °C. The hot deformation and subsequent aging modify the as-cast microstructure of $AlCoCrFeNi_{2.1}$. Long-term aging treatment forms B_2 precipitates, leading to outstanding tensile properties [34]. Strain induced precipitation of the B_2 phase was also reported by Zhang et al. [35] during hot tensile deformation of $AlCoCrFeNi_{2.1}$ HEA. Charkhchian et al. [36] showed that needle shape B_2 ordered phases are formed within the primary FCC region at high temperatures in a relatively short time.

The hot deformation behaviour of dual-phase FCC-based HEAs has been reported [26,29,37–44]. Discontinuous dynamic recrystallisation (DDRX) occurs at interfacial boundaries in the FCC phase by a mechanism involving Σ3 boundary formation and multiple twinning chain propagation [26,39]. In contrast, continuous dynamic recrystallisation (CDRX) occurs in the BCC phase [26]. The increase in anti-phase boundary energy between FCC/BCC phases is responsible for the increase in high-temperature strength in dual-phase FCC-based HEAs with Al. A rate-controlling hot deformation mechanism has been reported to be the solute drag effect of Al [45]. Although the recrystallisation mechanisms in dual-phase HEA are described, the interplay between the dynamic and static mechanisms in forming the microstructure during the thermomechanical processes needs to be further investigated.

This work aims to describe the role of the thermomechanical processing route on the microstructure modification and its correlation with the flow stress evolution for a dual-phase hypo-eutectic FCC-based HEA. The main objective is to provide a strategy for the microstructure design of similar HEAs by elucidating the strengthening and restoration mechanisms.

2. Experimental procedures

A high entropy alloy of 15Al, 14Co, 17.7Cr, 17.7Fe, 35.4Ni, 0.2Ti (at %) was cast using an induction-melting furnace. First, pure elemental metals were added to the melt, preheated to 1550 °C, under a protective atmosphere of Ar. The melt was then manually stirred and poured into a silica-based mould internally coated with aluminium oxide, preheated to 900 °C, and left cooled in air.

Cylindrical samples with 10 mm diameter and 15 mm length were cut along the solidification direction from the cast ingot. A Gleeble® 3800-GTC simulator was used for thermomechanical treatments. For temperature control, K-type thermocouples were welded to the specimens. A heating rate of 5 °C/s was used. Four types of thermomechanical treatments in the uniaxial compression direction were carried out:

a) Deformation at 1100 °C up to 0.85 strain for the strain rates of 0.001 s^{-1} and 1 s^{-1}. Two soak times of the 0.5 min and 3 min before deformation were used for 1 s^{-1}, while a soak of 3 min was used for 0.001 s^{-1}.
b) Strain rate jump tests at 1100 °C up to 0.85 strain from 0.001 s^{-1} to 1 s^{-1} and from 1 s^{-1} to 0.001 s^{-1} after reaching the strain of 0.425. Soaking before deformation: 3 min at 1100 °C.
c) Multi-stage deformation tests up to 0.85 strain at 1100 °C and 1 s^{-1}: each stage of deformation was equal to 0.05 strain, and the samples were held for 1 min or 5 min between the inter-stages of isothermal soaking. Soaking before deformation: 3 min at 1100 °C.
d) Deformation at 1000 °C and 0.1 s^{-1} up to 0.85 strain followed by annealing at 1150 °C for 30 min and 180 min in a furnace. Soak before deformation: 3 min at 1000 °C.

A sandwich of graphite and Mo foils was used between the specimen and the anvils to minimise the temperature gradient and friction during the tests. All specimens were water quenched immediately after testing to preserve the microstructure for further analysis. The specimens were sectioned along the compression direction and metallographically prepared by grinding to 2000 grit and polishing with colloidal silica suspension (OP-S).

Scanning electron microscopy (SEM), electron backscatter diffraction (EBSD) and energy dispersive X-ray spectroscopy (EDX) were used to examine the polished samples. An EDAX Apex system with a Hikari Plus EBSD camera was used for the EBSD measurements. EBSD maps were measured for the as-cast and deformed samples. OIM DataAnalysis 8.6 was used to analyse the EBSD data. Firstly, the confidence index of the grains was standardised to a minimum grain size of 5 pixels. Then the points with a confidence index below 0.2 were cleaned by correlation with the neighbours. A misorientation angle of 15° was considered as the transition angle between low and high angle grain boundaries. The average grain misorientation was obtained using the first nearest neighbour. The Σ3 boundaries were calculated using a tolerance of $15 \cdot ("\Sigma")^{0.5}$. Grain orientation spread was calculated considering a grain surrounded by high angle grain boundaries (misorientation angle greater than 15°).

3. Results

3.1. As-cast microstructure

The as-cast microstructure of the investigated alloy is composed of two phases, as shown in Fig. 1. The overall microstructure corresponds to a hypo-eutectic alloy. The Al and Ni rich phase is indexed in the EBSD measurements according to a general BCC structure, hereon named “Eutectic BCC phase”, as shown in green in the EBSD phase map in Fig. 1f. The matrix enriched in Co, Fe and Cr is indexed in the EBSD measurements according to an FCC crystal structure, hereon named “FCC phase”, as shown in red in Fig. 1f. The elemental partition is explained is a characteristic of the eutectic behaviour of the alloy system [36,46,47]. The FCC has large grains, as shown in Fig. 1g, while the eutectic BCC phase is arranged into colony-like eutectic structures of smaller size, Fig. 1h. The black arrows in Fig. 1(a-e) indicate Al-rich oxide inclusions within the FCC matrix.

3.2. Hot deformation at constant strain rate and strain rate jump

The flow curves at constant strain rates and after strain rate jumps are shown in Fig. 2. Fig. 2(a and b) show the flow curves after deformation at 1000 °C and 1100 °C, respectively. Fig. 2a shows the plastic region of the flow curves for three different samples tested at 1000 °C and 0.1 s^{-1}. Although the overall evolution of the flow stress is comparable, the absolute values of the flow stresses differ by up to 30 %. The strain at the peak stress also varies. The large as-cast FCC grains shown in Fig. 1 explain the dependence of the yield stress on the sample. The critical resolved shear stress and the work hardening are related to the crystallographic orientation via the Schmid factor. Therefore, as shown in Fig. 2a, the applied strain rate can produce different stress values when only a few grains are present in each sample.

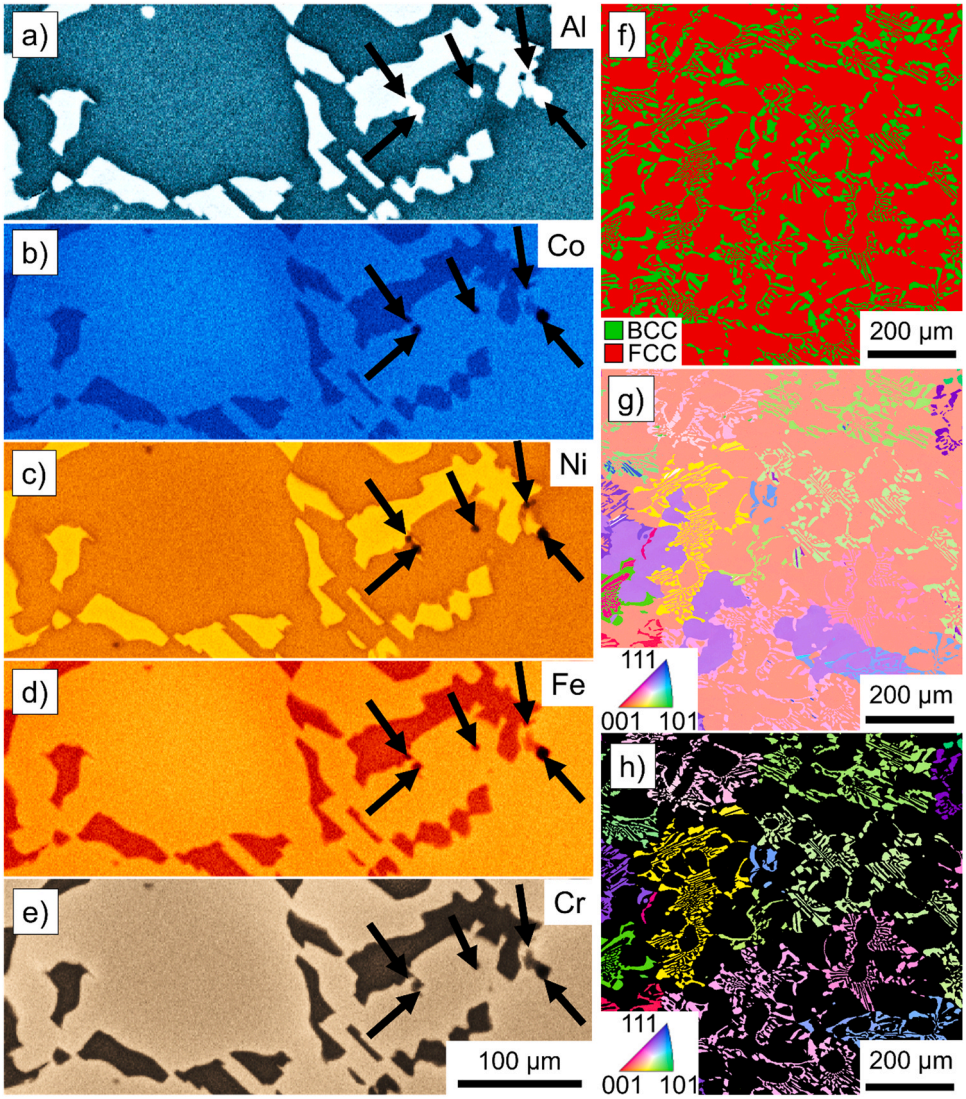

Fig. 1. As-cast microstructure of the investigated high entropy alloy: a-e) EDX maps of a) Al; b) Co; c) Ni; d) Fe; e) Cr; and results of the EBSD measurements: f) phase map; g) inverse pole figure (IPF); h) IPF of the eutectic BCC-phase. The black arrow in (a-e) indicates oxide inclusions.

Rapid work hardening followed by peak stress and flow softening occurs for all temperatures and constant strain rates. Fig. 2b shows the flow curves after the strain rate jump:

- from 0.001 s^{-1} to 1 s^{-1}: the work hardening that occurred during the first deformation increases the yield stress for the second deformation at 1 s^{-1}.

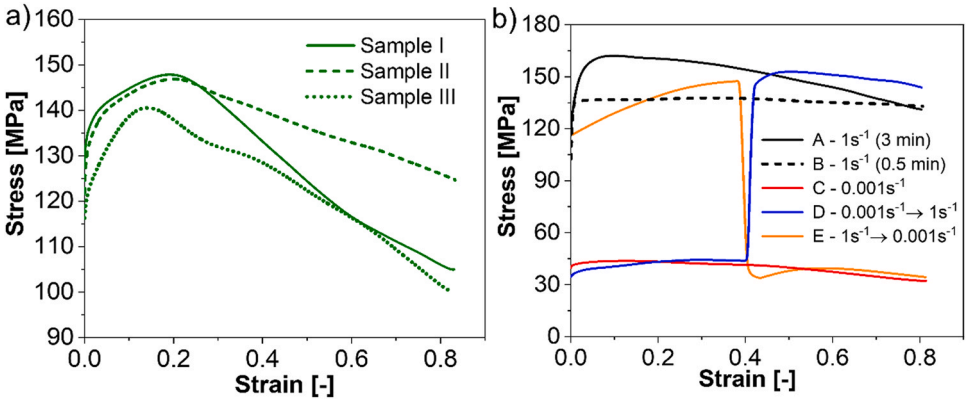

Fig. 2. Flow curves for the hot compression tests performed at a) the plastic region for three repetitions (Samples I to III) at 1000 °C and 0.1 s^{-1}; b) 1100 °C and: A) at the constant strain rate of 1 s^{-1} for a soak time prior to deformation of 3 min; B) at the constant strain rate of 1 s^{-1} for a soak time prior to deformation of 0.5 min as well as for strain rate jump; C) at the constant strain rate of 0.001 s^{-1} for a soak time prior to deformation of 3 min; D) at strain rate jump from 0.001 s^{-1} to 1 s^{-1} for a soak time prior to deformation of 3 min; E) at strain rate jump from 1 s^{-1} to 0.001 s^{-1} for a soak time prior to deformation of 3 min.

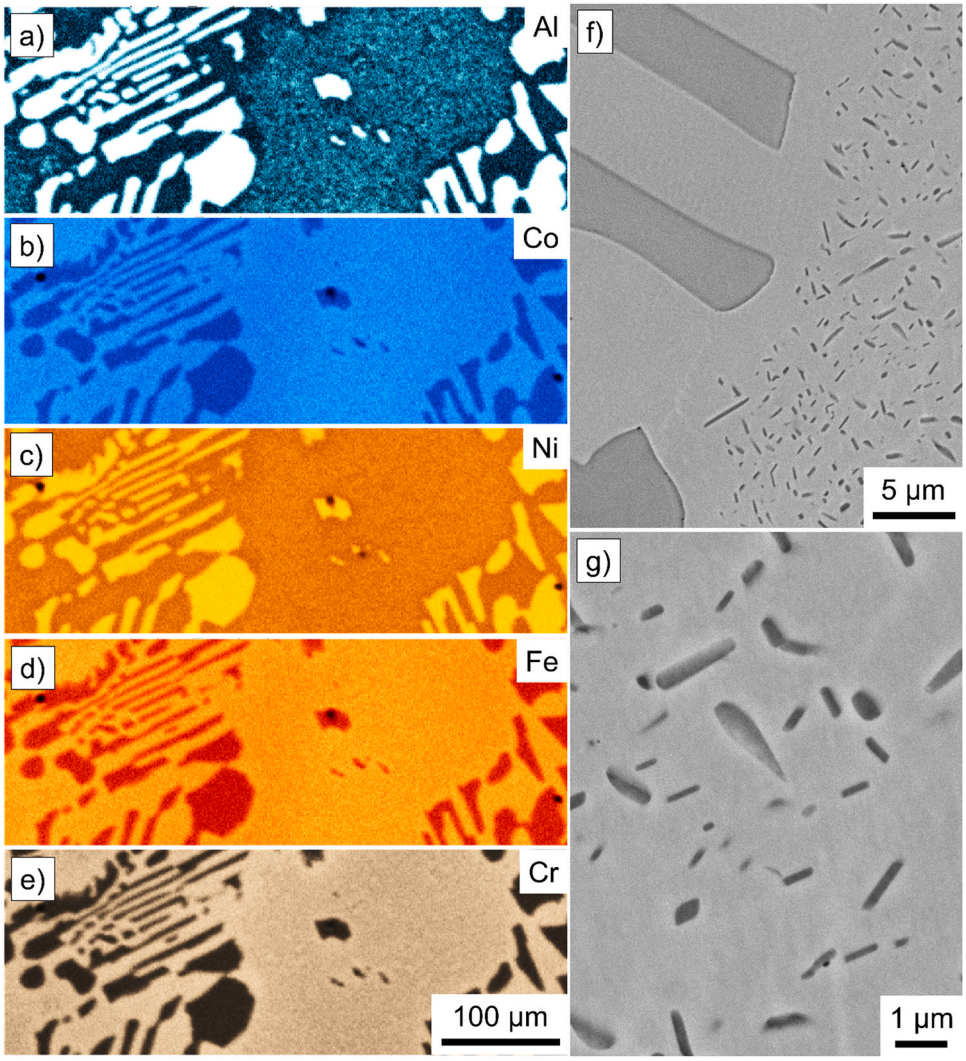

Fig. 3. Microstructure of the alloy immediately before deformation at 1100 °C after 3 min holding: a-e) energy dispersive X-ray spectroscopy (EDX) maps of a) Al; b) Co; c) Ni; d) Fe; e) Cr; and f,g) backscattered electron (BSE) micrographs.

- from 1 s^{-1} to 0.001 s^{-1}: the stresses reached during the first step of deformation at 1 s^{-1} are rapidly relaxed during the second step at 0.001 s^{-1}. The stresses start at a value like the yield stress of the flow curve of the test at the constant strain rate of 0.001 s^{-1}.

These tests show that it is only when jumping from low to high strain rates that the microstructural features produced during deformation are dependent on the deformation parameters. Time (strain) is required to recover the microstructure in the early stages of the second step when jumping from high to low strain rates.

The flow curves shown in Fig. 2b were obtained for hot compression tests carried out after soaking for 3 min before deformation. The dashed black line at 1 s^{-1} was obtained when the pre-strain soak was 0.5 min and showed rapid work hardening followed by less flow softening and lower stress values compared to the test at 1 s^{-1} after 3 min soak.

Fig. 3 shows the microstructure of the alloy after 3 min at 1100 °C. An Al rich phase precipitates within the FCC matrix, as shown in Fig. 3(a,f,g), indicating that the as-cast microstructure was not at thermodynamic equilibrium prior to hot deformation. The formation of micro-scale precipitates in the inter-dendritic region is also in agreement with the findings of Charkhchian et al. [36]. As suggested in literature, the micro-scale precipitates likely have a BCC crystal structure, which was used for their EBSD indexation. The micro-scale precipitates are hereon named “Secondary phase”. Although sluggish diffusion was reported for HEAs [48], it is mainly associated with Mn presence [49]. There is no Mn in the current alloy. Thus, all associated phenomena with diffusion are expected to be like the conventional alloy systems, explaining the relatively fast precipitation kinetics for the investigated alloy.

Fig. 4 shows the effect of strain rate and soaking time prior to deformation on the FCC microstructure (deformation at 1100 °C up to 0.85 of strain). Some new HAGBs are formed in the FCC phase, as well as many LAGBs. Plastic deformation bends the crystal structure of the grains, creating a misorientation gradient. At the strain rate of 0.001 s^{-1}, there is more time for recrystallisation (Fig. 4(c,f))

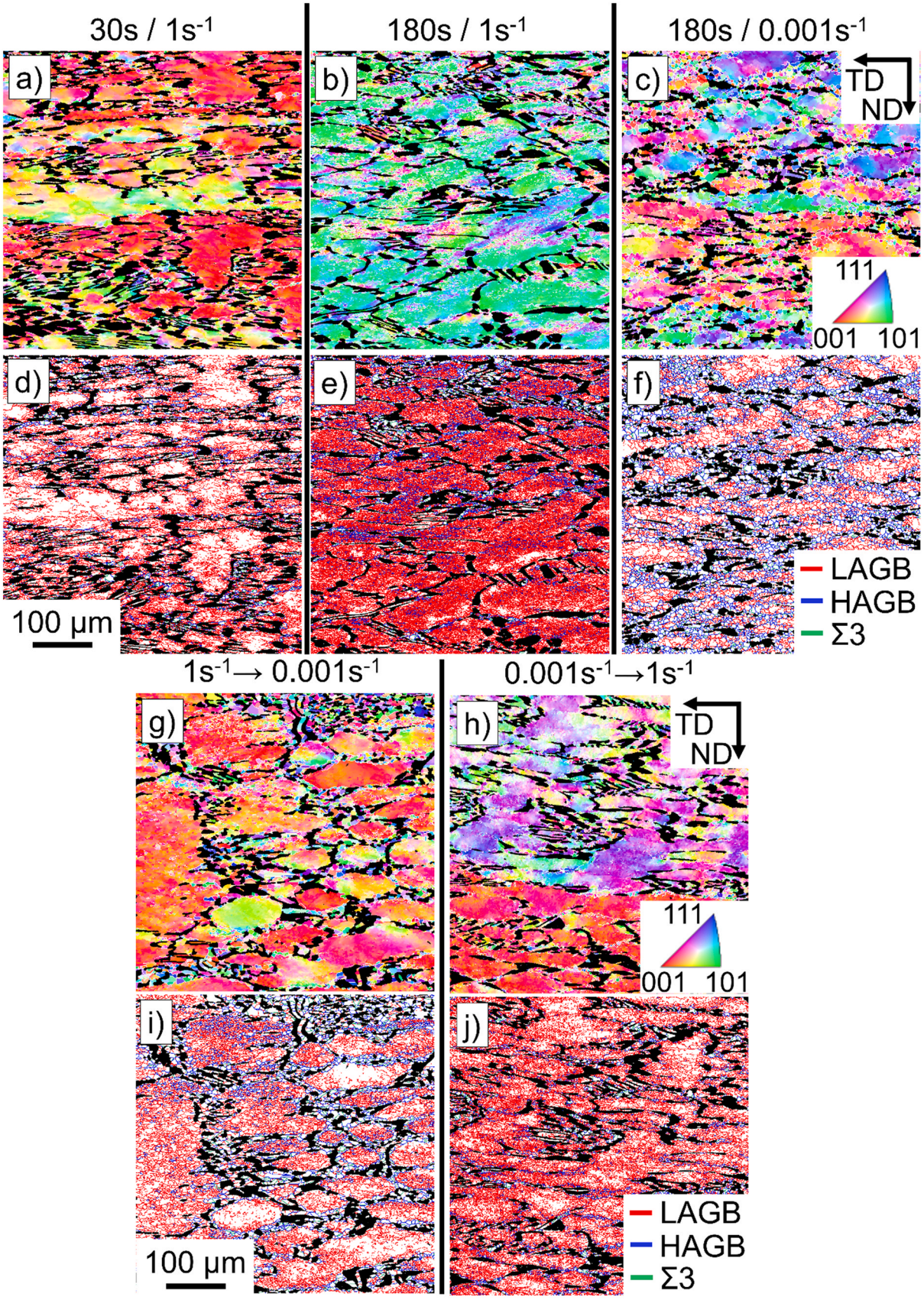

Fig. 4. Electron backscattered diffraction (EBSD) maps of the FCC-phase for the samples deformed at 1100 °C and: a,d) 1 s^{-1} after soaking before deformation for the 0.5 min; b,e) 1 s^{-1} after soaking before deformation for 3 min; c,f) 0.001 s^{-1} after soaking before deformation for 3 min; g,i) strain rate jump from 1 s^{-1} to 0.001 s^{-1} after soaking before deformation for 3 min; h,j) strain rate jump from 0.001 s^{-1} to 1 s^{-1} after soaking before deformation for 3 min. The: a-c,g,h) are the inverse pole figure maps; and d-f,I,j) the boundary maps. The white lines in the IPF maps indicate all the HAGBs.

compared to 1 s^{-1} in Fig. 4(b,e). Longer soak time produced a finer substructure, as seen in Fig. 4(b,e), compared to the deformation after the 0.5 min soak time shown in Fig. 4(a,d).

The substructure of the sample deformed at the strain rate jump from 1 s^{-1} to 0.001 s^{-1} (Fig. 4(g,i)) is similar to that of the hot compression at the constant strain rate of 0.001 s^{-1} (Fig. 4(c,f)). The difference is that a higher density of HAGBs is observed at the constant strain rate of 0.001 s^{-1} in Fig. 4(c,f). It indicates that the microstructure produced at the strain rate jump from 1 s^{-1} to 0.001 s^{-1} correspond to an early stage of recrystallisation compared to the one produced at the constant strain rate of 0.001 s^{-1}. A similar result can be seen by comparing the deformation at a constant strain rate at 1 s^{-1} (Fig. 4(b,e)) and after the strain rate jump from 0.001 s^{-1} to 1 s^{-1} (Fig. 4(h,j)). Thus, the alloy under investigation appears to have little dependence on the thermomechanical history. The deformation state at the last step determines the final microstructure. In the case of the strain rate jump, the microstructure formed in the first step is modified according to the strain rate of the second step. As the jump occurs at the strain of 0.425, a higher total strain would be required to achieve a similar microstructure to that formed at a constant strain rate, as shown in Fig. 4(b,c,e,f).

Fig. 5 shows high-resolution EBSD measurement maps for regions within the FCC matrix for the hot compression at 1100 °C. The black areas correspond to the regions indexed as the BCC phase formed within the FCC matrix, as shown in Fig. 3. Comparing the microstructures shown in Fig. 5, the following can be interpreted:

- Misorientation spread within the FCC substructure is present in most grains and is more pronounced at 1 s^{-1}. The progressive misorientation change can be seen in the rotational axis given by the grain reference orientation deviation (GROD) axis maps in Fig. 5(c,f,i,l,o).
- High KAM values in Fig. 5(b,e,h,k,n) correspond to boundaries where a sharp change in the GROD axis is visible in Fig. 5(c,f,i,l,o).
- The precipitates formed during soaking are typically located along FCC grain boundaries or regions with sharp changes in rotation axis of the FCC phase. The precipitates formed after soaking before deformation globularise and coarsen at low strain rates (Fig. 5(g-i)). The precipitates formed after soaking are larger after deformation at the strain rate jump from 0.001 s^{-1} to 1 s^{-1} than those formed at the constant strain rate of 1 s^{-1}. In general, the longer deformation time, the larger the fraction of the secondary phase.
- The substructure formed for the strain rate jump from 1 s^{-1} to 0.001 s^{-1} is comparable to the one formed at the constant strain rate of 0.001 s^{-1}. Moreover, the substructure after the constant strain rate of 1 s^{-1} is finer than the rate jump from 0.001 s^{-1} to 1 s^{-1} and lower from 1 s^{-1} to 0.001 s^{-1} compared to its final strain rates.
- The density of LAGBs and HAGBs in the FCC phase is higher in the case of 3 min soaking (Fig. 5(d-f)) than in the 0.5 min one (Fig. 5(a-c)). Some regions are only surrounded by HAGBs with Σ3 boundaries in the interior, while others are surrounded by both HAGBs and/or LAGBs. Overall, a negligible amount of Σ3 boundaries is formed by DDRX compared to LAGBs and HAGBs.

Thus, the secondary phase formed within the FCC matrix is largely responsible for the higher work hardening after 3 min soaking when comparing the hot compression tests after 0.5 min

The flow softening observed in Fig. 2 results from I) the interaction between the restoration mechanisms in each phase and II) the change in load partitioning between them. The plastic deformation also modifies the microstructure of the eutectic BCC phase, as shown in Fig. 6. Fig. 6(d,e,j) shows that the eutectic BCC phase stored the plastic deformation by bending its crystal structure and forming regions with high KAM values for the constant strain rate of 1 s^{-1} and the strain rate jump from 0.001 s^{-1} to 1 s^{-1}. Fig. 6(a,b,h) shows that there is no pronounced change in the orientation between the neighbouring particles for the constant strain rate of 1 s^{-1} and the strain rate jump from 0.001 s^{-1} to 1 s^{-1}. In addition, there is no visible difference between the deformation at 1 s^{-1} after 0.5 min soaking (Fig. 6(a,d)) and 3 min soaking (Fig. 6(b,e)).

The restoration mechanisms have time to modify the microstructure at 0.001 s^{-1}, although the stored energy is smaller, as the time to achieve the same strain is a thousand times longer at 0.001 s^{-1} than at 1 s^{-1}. Fig. 6 f shows some regions with high KAM values after hot compression at 1100 °C and 0.001 s^{-1} and a more globularised eutectic BCC phase compared to the same features formed after deformation at 1 s^{-1}, Fig. 6(d,e). The microstructure formed after the strain rate jump from 1 s^{-1} to 0.001 s^{-1} (Fig. 6(g,i)) is similar to that formed after the constant strain rate at 0.001 s^{-1} (Fig. 6(c,f)). Like the results for the FCC phase, the eutectic BCC phase shows a microstructure that accommodates the plastic deformation according to the actual parameters (strain rate and temperature) of the deformation, regardless of the thermomechanical history.

3.3. Multi-stage deformation

A typical industrial thermomechanical process can involve multiple deformation steps and soaking between the deformation steps, provoking complex interactions between the dynamic and static restoration mechanisms. To elucidate the role of these mechanisms, multi-stage deformation tests were performed at 1100 °C for a strain rate of 1 s^{-1}. Fig. 7(a and c) show the true stress-strain curves for the tests performed with a soaking step of the 1 min and 5 min, respectively, between the deformation steps. Fig. 7(b,d) shows the stress evolution as a function of the time for the same tests. The following results can be interpreted from Fig. 7:

- The stresses achieved during deformation decrease with increasing strain.
- The minimum stress reached during soaking between the deformation steps decreases with increasing strain.
- The softening described above was more pronounced for the 5 min soak time than for the 1 min soak.

Assuming that the total strain during an isothermal test is the sum of elastic and plastic strains, Eq. (1) and Hook's law can calculate the plastic strain according to Eq. (2). Furthermore, assuming that in the derivative of Hook's law, the plastic strain rate as a function of the stress evolution can be expressed by Eq. (3).

$$\varepsilon = \varepsilon_p + \varepsilon_e \tag{1}$$

$$\varepsilon_p = -\frac{\sigma}{E} \tag{2}$$

$$\dot{\varepsilon}_p = -\frac{\dot{\sigma}}{E} \tag{3}$$

Using an estimated Young modulus of 160 GPa for the high entropy alloy [50], the calculated plastic strain rate over the stress is shown in Fig. 8(a and c) for the 1 min and 5 min interstage, respectively. At high stresses, the plastic strain rate is up to one order

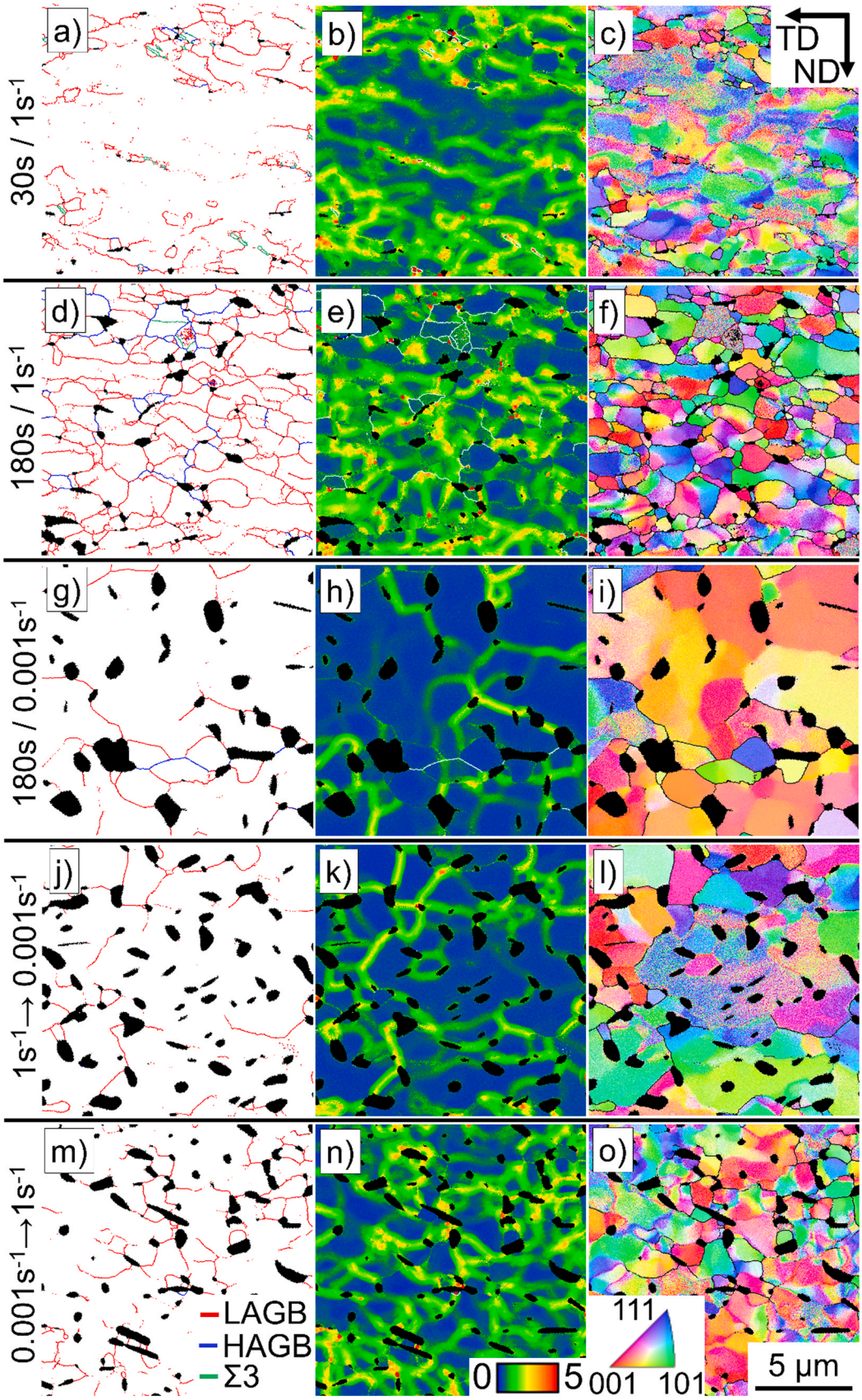

Fig. 5. Electron backscattered diffraction (EBSD) maps of the FCC-phase for the samples deformed at 1100 °C and: a-c) 1 s^{-1} after 0.5 min soaking before the deformation; d-f) 1 s^{-1} after 3 min soaking before the deformation; g-i) 0.001 s^{-1} after 3 min soaking before the deformation; j-l) strain rate jump from 1 s^{-1} to 0.001 s^{-1} after 3 min soaking before the deformation; m-o) strain rate jump from 0.001 s^{-1} to 1 s^{-1} after 3 min soaking before the deformation; showing the: a,d,g,j,m) boundary maps; b,e,h,k,n) KAM maps; c,f,i,l,o) grain reference orientation deviation (GROD) axis. The black and white lines in the GROD and KAM maps indicate all the high-angle grain boundaries.

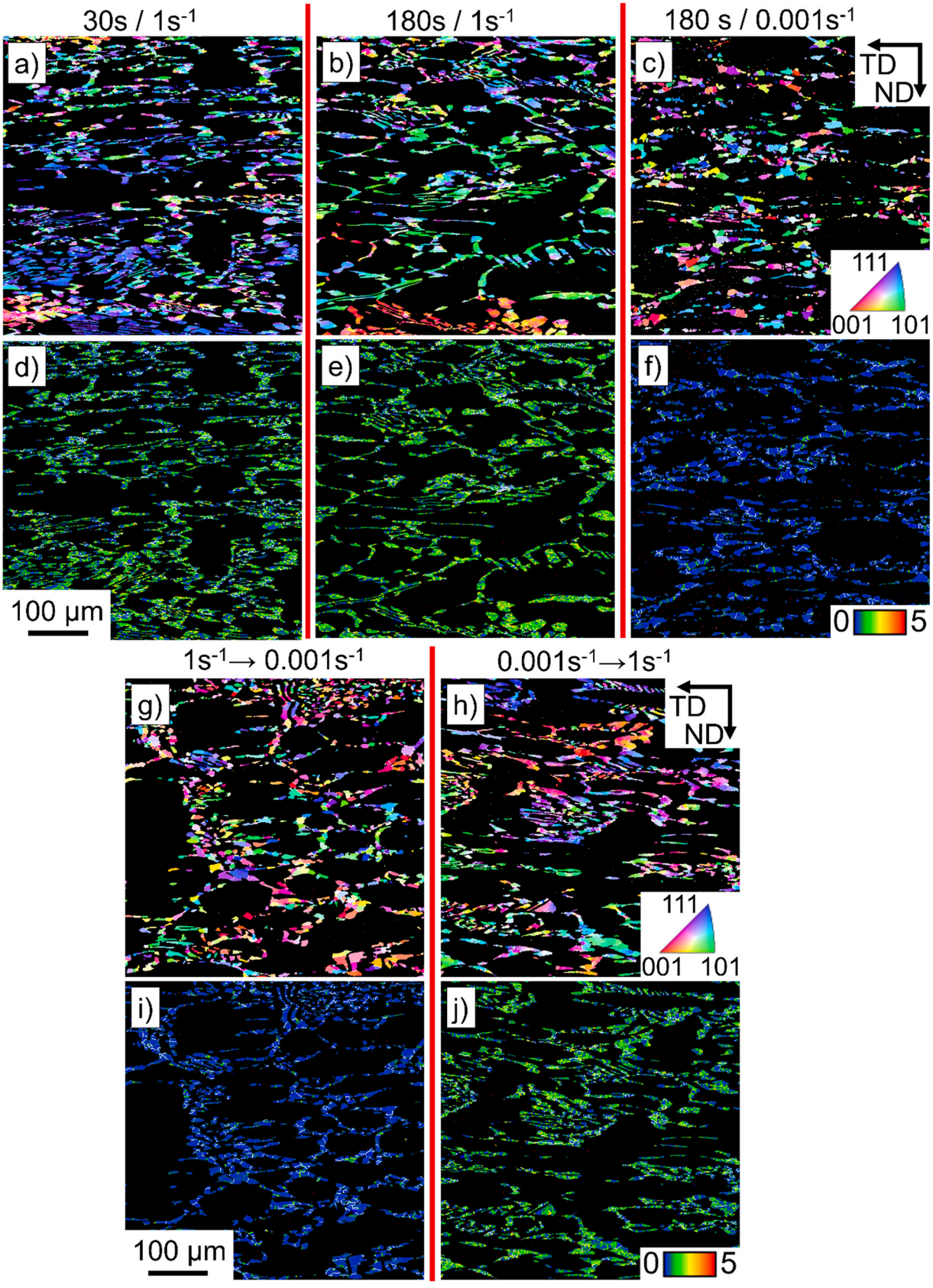

Fig. 6. Electron backscattered diffraction (EBSD) maps of the eutectic BCC phase for the samples deformed at 1100 °C and: a,d) 1 s^{-1} after soaking before deformation for the 0.5 min; b,e) 1 s^{-1} after soaking before deformation for 3 min; c,f) 0.001 s^{-1} after soaking before deformation for 3 min; g,i) strain rate jump from 1 s^{-1} to 0.001 s^{-1} after soaking before deformation for 3 min; h,j) strain rate jump from 0.001 s^{-1} to 1 s^{-1} after soaking before deformation for 3 min; showing the: a-c,g,h) inverse pole figure maps; d-f,i,j) kernel average misorientation (KAM) maps. The white lines in the inverse pole figure and KAM maps indicate all the high-angle grain boundaries.

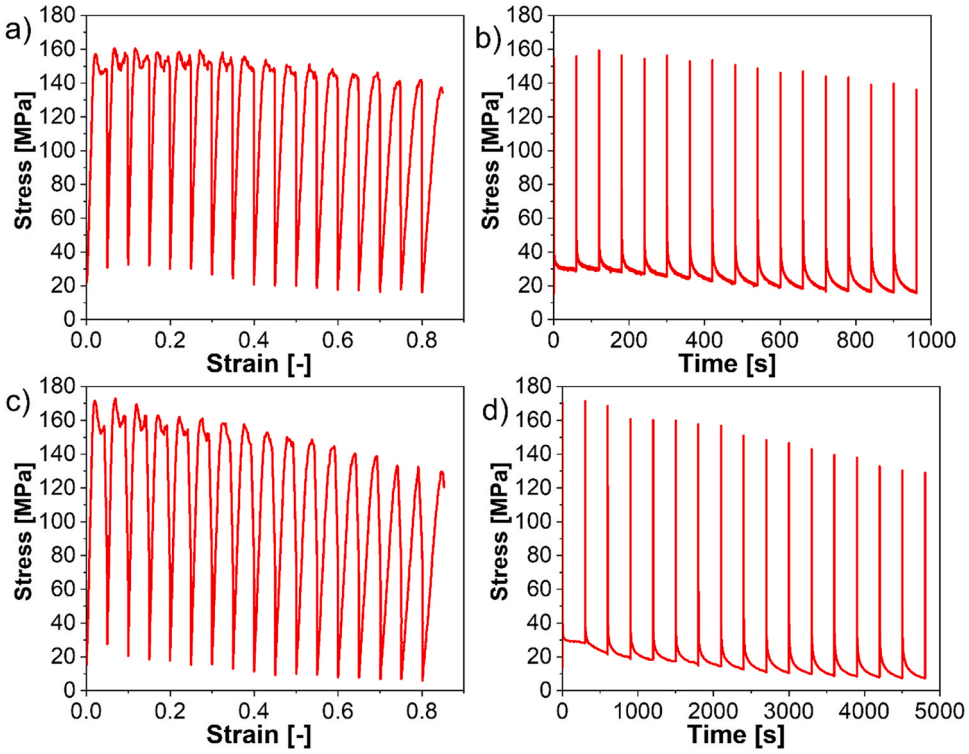

Fig. 7. a,c) flow stress for the tested alloy with the inter-stage period of the 1 min and 5 min, respectively; b,d) true stress evolution for the tested alloy with the inter-stage period of 1 min and 5 min, respectively.

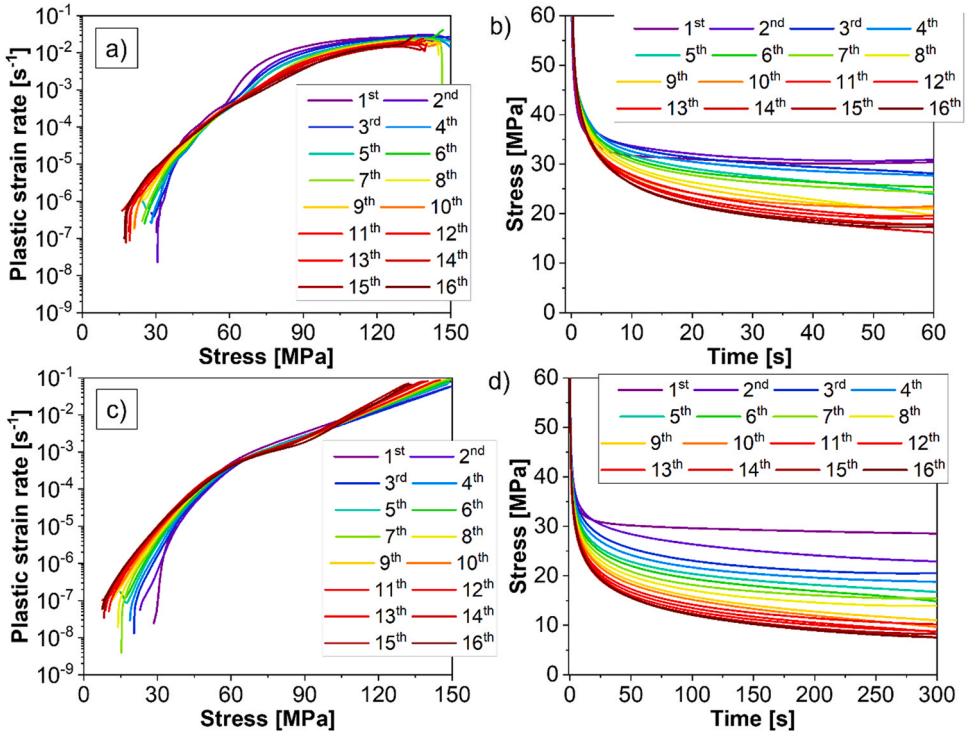

Fig. 8. Stress relaxation results: a,c) plastic strain rate evolution for the test with the inter-stage period of 1 min and 5 min, respectively; b,d) stress evolution for the inter-stage period of 1 min and 5 min, respectively.

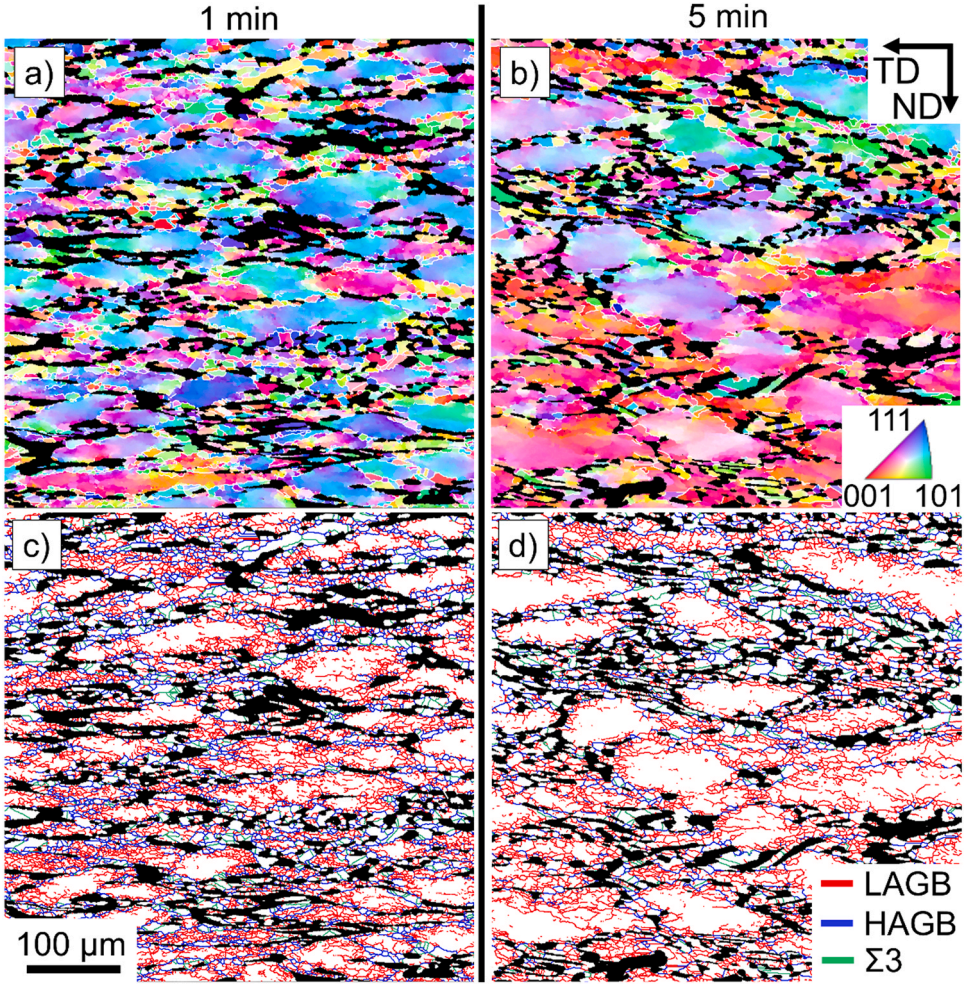

Fig. 9. Electron backscattered diffraction (EBSD) maps of the FCC phase deformed at 1100 °C and 1 s^{-1} for the inter-stage period of a,c) the 1 min; b,d) 5 min, showing: a,b) inverse pole figure maps; c,d) boundary maps. The white lines in the inverse pole figure maps indicate the high-angle grain boundaries.

of magnitude greater in the early stages of deformation than in the latter stages. This tendency applies only to the short soak time. The opposite is true for the 5 min soak time between deformations. The calculated plastic strain rate decreases sharply for the first deformation steps as the stresses relax (left part of the diagram). In contrast, for the same values of plastic strain rate, lower values of stresses are reached after the last deformation steps.

Fig. 8(b,d) shows the stress relaxation versus time. The stress of ~30 MPa is reached after ~45 s of relaxation after the first deformation step. Increasing the deformation steps: I) lower stresses are reached during soaking; II) longer times are required to reach steady state. The stress-relaxation rate increases with the number of deformation steps. This rate increase is smaller from one deformation step to the next one.

Overall, Fig. 7 and Fig. 8 show that the material becomes softer as the deformation step increases and the steady state stress relaxation is reached at longer times. This behaviour is closely related to the microstructural evolution during the multi-stage deformation test. The FCC microstructures after the tests are shown in Fig. 9. A high density of HAGBs, particularly Σ3 boundaries, were formed by recrystallisation compared to the material deformed at the same strain rate without inter-stage soaking. The density of LAGBs is lower than in the tests performed at constant strain rates or with strain rate jumps shown in Fig. 4, especially compared to the test performed at 1 s^{-1} (Fig. 4(b,e)).

Fig. 9 shows that the LAGBs network is slightly denser for the inter-stage holding of the 1 min compared to the 5 min Fig. 10 shows high-resolution EBSD measurement maps of the FCC phase for the central regions of the prior FCC grains confirming the previous statement concerning boundaries, local misorientation (KAM) and grain rotation (GROD). Defined regions with slight differences in rotation axis are shown in Fig. 10f for 5 min inter-stage holding as indicated by the yellow arrows. In contrast, finer regions with a progressive change in rotation axis associated with misorientation spread are shown in Fig. 10c for 1 min inter-stage holding, as indicated by the blue dashed ellipses. Thus, 1 min of inter-stage

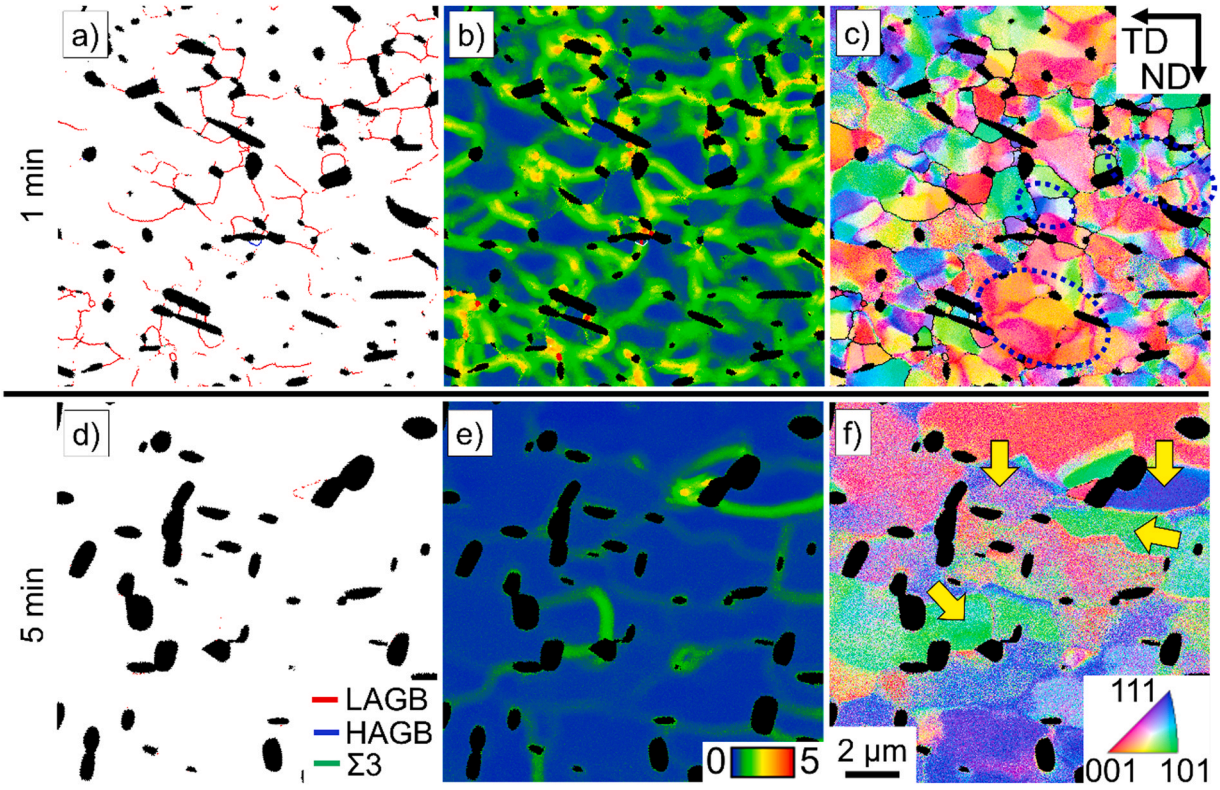

Fig. 10. Results of the Electron backscattered diffraction (EBSD) measurements of the FCC phase deformed at 1100 °C and 1 s^{-1} with an inter-stage period of a,c,e) The 1 min; b,d,f) 5 min, showing the: a,b) boundary maps; c,d) KAM maps; e,f) GRO) maps. The black lines in the GROD maps indicate all the high-angle grain boundaries. Blue dashed arrows in c) indicate regions with misorientation spread. Yellow arrows in f) indicate defined regions with small differences in the rotation axis.

holding is insufficient to significantly annihilate dislocations and reduce the misorientation spread in the central regions of the prior FCC grains, achieved at 5 min

Fig. 11 shows the microstructure of the eutectic BCC phase after multi-stage hot compression. Compared to the IPF and KAM maps obtained for a constant strain rate of 1 s^{-1} shown in Fig. 6(b,e), Fig. 11 shows a more recrystallised and partially globularised eutectic BCC phase, especially for the multi-stage holding test of 5 min, Fig. 11(b,d). Longer multi-stage holding times enhance the restoration by recovery and recrystallisation of the FCC matrix, as well as the recrystallisation and globularisation of the eutectic BCC phase.

3.4. Microstructure evolution during annealing

Although new HAGBs and new grains are formed in the FCC matrix for the constant strain rate, strain rate jump and multi-stage tests, none successfully refine the FCC as-cast grain structure up to the tested strain. Fig. 12 shows the EBSD maps after hot compression at 1000 °C and 0.1 s^{-1} (Fig. 12(a,d,g)) followed by annealing at 1150 °C for 30 min (Fig. 12(b,e,h)) and 180 min (Fig. 12(c,f,i)). Fig. 12a,d shows a fine substructure formed within the FCC phase without new recrystallised grains. This substructure carries high stored energy in KAM, as shown in Fig. 12g. Some static recrystallised grains, more prominent along the interfaces with the deformed eutectic BCC phase, can be observed after 30 min of annealing. The substructure of the FCC matrix is largely preserved as shown in Fig. 12(e,h). The long annealing time of 180 min results in a partially recrystallised microstructure. The static recovery also annihilates and rearranges dislocations, slightly reducing the KAM values (Fig. 12i) and the stored energy within the FCC phase.

4. Discussion

4.1. Dynamic restoration mechanisms

This section discusses the metallurgical changes that occur during the hot deformation of both phases. Fig. 13 shows the EBSD maps of the BCC and FCC EBSD indexed phases after deformation at 1100 °C and 0.001 s^{-1} and 1 s^{-1}. The density of LAGBs formed in both BCC and FCC phases after deformation at 1 s^{-1} (Fig. 13(e and g, respectively)) is larger than that after deformation at 0.001 s^{-1} (Fig. 13(a,c)). The density of HAGB in the FCC phase is larger at 0.001 s^{-1} (Fig. 13c) than 1 s^{-1} (Fig. 13g). The GROD axis maps in Fig. 13(b,f) show that each region surrounded by LAGBs and HAGBs in the eutectic BCC phase has a different rotation axis to the neighbouring regions. Misorientation spread is also present within the eutectic BCC phase at 1 s^{-1}. Thus, the plastic deformation forms boundaries and misorientation within the eutectic BCC phase. Progressive lattice rotation and extensive dynamic recovery increase boundary misorientation, forming new HAGBs by CDRX. The CDRX is accompanied by a progressive fragmentation of the semi-continuous eutectic BCC network, modifying the stress and strain distributions

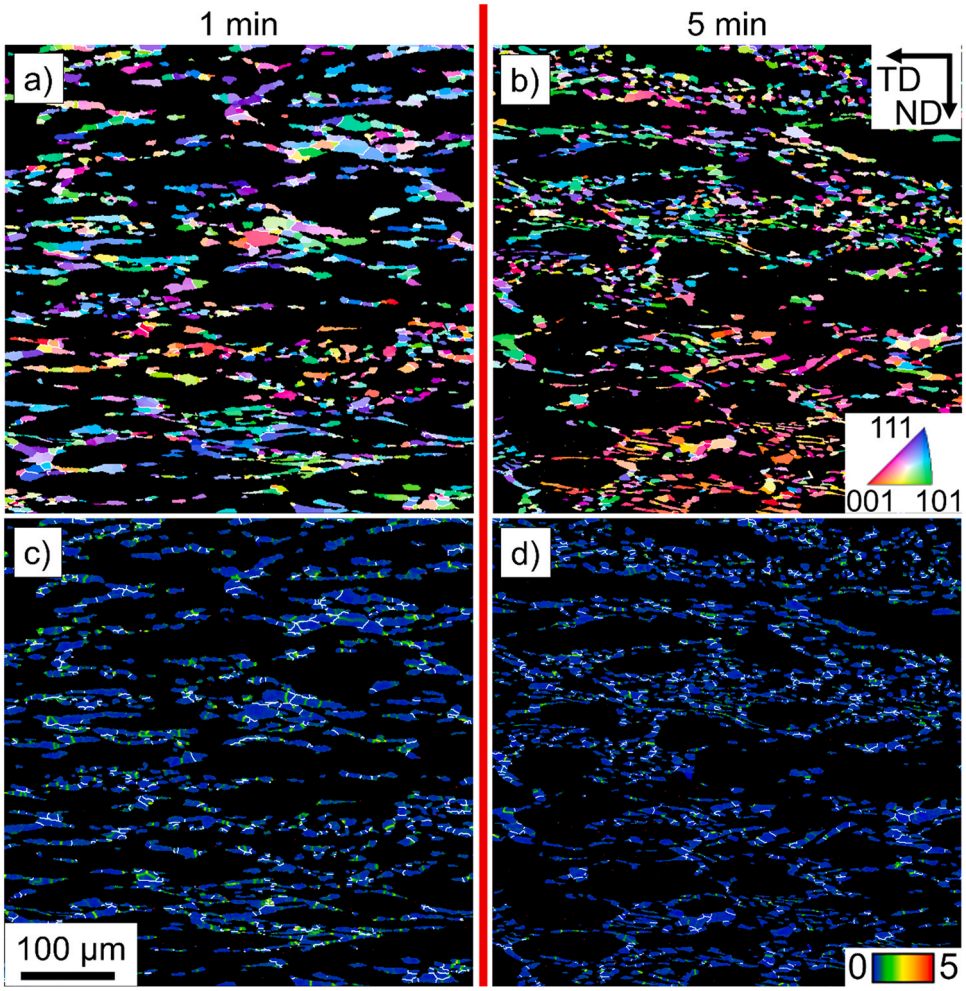

Fig. 11. Results of electron backscattered diffraction measurements of the eutectic BCC phase deformed at 1100 °C and 1 s^{-1} with an inter-stage period of a,b) the 1 min; c,d) 5 min, showing the: a,c) inverse pole figure maps; c,d) kernel average misorientation maps. The white lines in the IPF and KAM maps indicate all the high-angle grain boundaries.

within the material. The overall flow behaviour observed for the investigated alloy is a result of the following:

- Progressive fragmentation of the eutectic BCC network
- Progressive rearrangement of the dislocations within the FCC matrix that were formed in the early stages of the deformation. The eutectic BCC phase and the secondary phase can act as a dislocation source. They contribute to the high dislocation density in the early stages.
- The eutectic BCC particles contribute to the lattice rotation, which can promote a faster dislocations rearrangement, allowing a faster the substructure formation.
- Discontinuous dynamic recrystallisation (DDRX), i.e., nucleation and growth of the new grains, in the FCC phase was limited to the regions close to the eutectic BCC interface where local lattice rotation in the FCC phase is promoted.
- The DDRX grains of the FCC phase continue to deform.

4.2. Static restoration mechanisms

Static recrystallisation is slow. Fig. 12 shows that after 180 min recrystallisation is still incomplete. Fig. 14(a,b) shows the FCC microstructure of the alloy deformed at 1100 °C and 0.001 s^{-1}, and Fig. 14(e,f) shows the FCC microstructure of the alloy deformation at 1100 °C and 0.1 s^{-1} followed by annealing at 1150 °C for 180 min. DDRX occurs by forming Σ3 boundaries. The nucleation and growth of new grains is hindered in the regions in which the secondary phase is present. The high GOS values in Fig. 14(c,g) are explained by the low KAM values in the eutectic BCC phase (Fig. 14(d,h)) but the presence of LAGBs instead of just HAGBs. It indicates that full recrystallisation was not achieved due to I) insufficient time/deformation for CDRX in the case of deformation only, Fig. 14(c,d); II) insufficient stored energy in the case of static recrystallisation, Fig. 14(g,h).

Fig. 15 shows a detailed view of a region where a nucleus is forming and growing, creating Σ3 boundaries that consume the high KAM regions. As shown in Fig. 15a, the intersection of Σ3 with other Σ3 boundaries can form a Σ9 boundary.

4.3. Role of the eutectic BCC phase and secondary phase on the deformation behaviour

The investigated high entropy alloy consists of a percolated matrix of FCC phase with eutectic BCC phase indexed in the EBSD

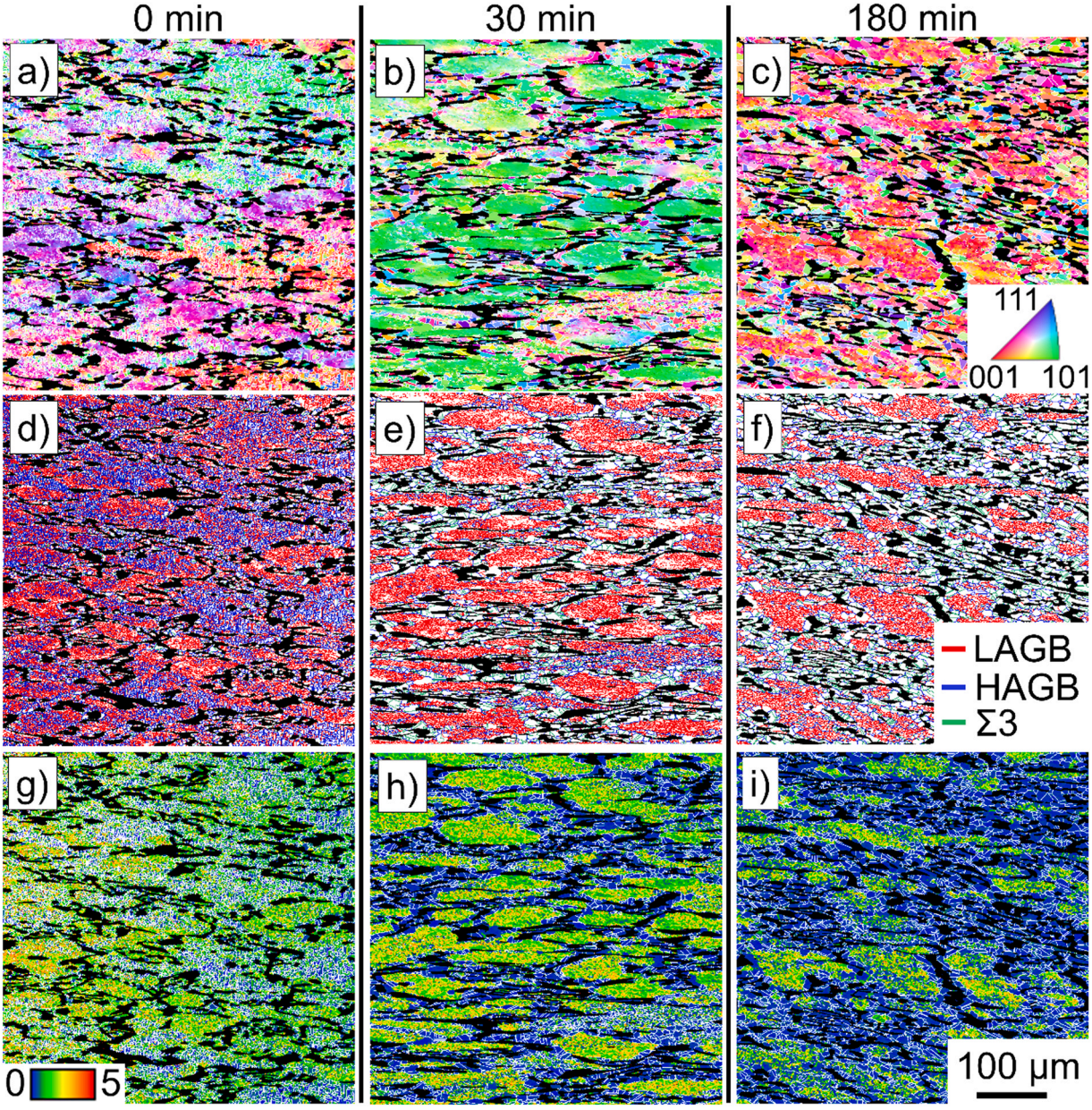

Fig. 12. Results of the electron backscattered diffraction measurements of the FCC phase deformed at 1000 °C and 0.1 s^{-1} and annealed at 1150 °C for: a,c,e) 0 min (as-deformed); b,d,f) 30 min; c,f,i) 180 min, showing the: a-c) inverse pole figure maps, d-f) boundary maps, g-i) kernel average misorientation maps. The white lines in the IPF and KAM maps indicate the high-angle grain boundaries.

measurements and secondary phases formed during soaking and/or deformation, also indexed as BCC phase in the EBSD measurements. Fig. 16 shows the characteristic morphologies of the secondary phase after the tests carried out in this work. The secondary phase that precipitated within the FCC matrix during soaking prior to deformation are finer after soaking for 0.5 min (Fig. 16a) than after soaking for 3 min (Fig. 16b). The coarsening of the secondary phase (Fig. 16b compared to Fig. 16c) is promoted by increasing the deformation time (decreasing the strain rate). Increasing the deformation time (decreasing the strain rate) promotes secondary phase coarsening. The secondary phase formed for the strain rate jump tests at 1100 °C (Fig. 16 (d,e)) are comparable to each other and are slightly smaller than those formed at 0.001 s^{-1} (Fig. 16c). The secondary phase coarsens during the multi-stage tests at 1100 °C (Fig. 16 (f,g)). Annealing at 1150 °C for 30 min and 180 min after deformation also coarsened the secondary phase (Fig. 16I and Fig. 16j, respectively).

The secondary phase that precipitate is rich in Al and Ni, like the deformed eutectic BCC phase, as shown in Fig. 17 for the hot compression at 1100 °C and 0.001 s^{-1}. These fine particles of the

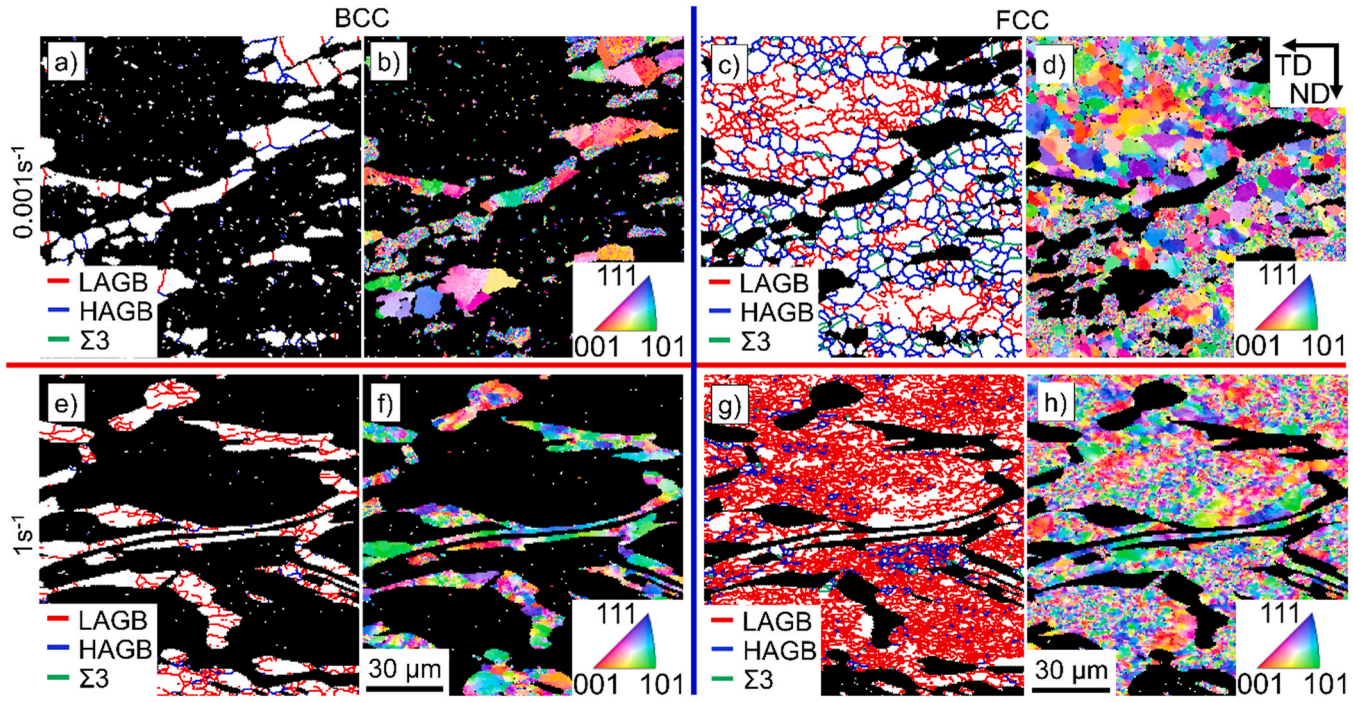

Fig. 13. Electron backscattered diffraction (EBSD) maps of the BCC phase for the samples deformed at 1100 °C and: a-d) 0.001 s^{-1}; e-h) 1 s^{-1}; showing the: a,e,c,g) boundary maps; b,d,f,h) grain reference orientation deviation (GROD) axis maps; for the a,b,e,f) BCC phase; c,d,g,h) FCC phase.

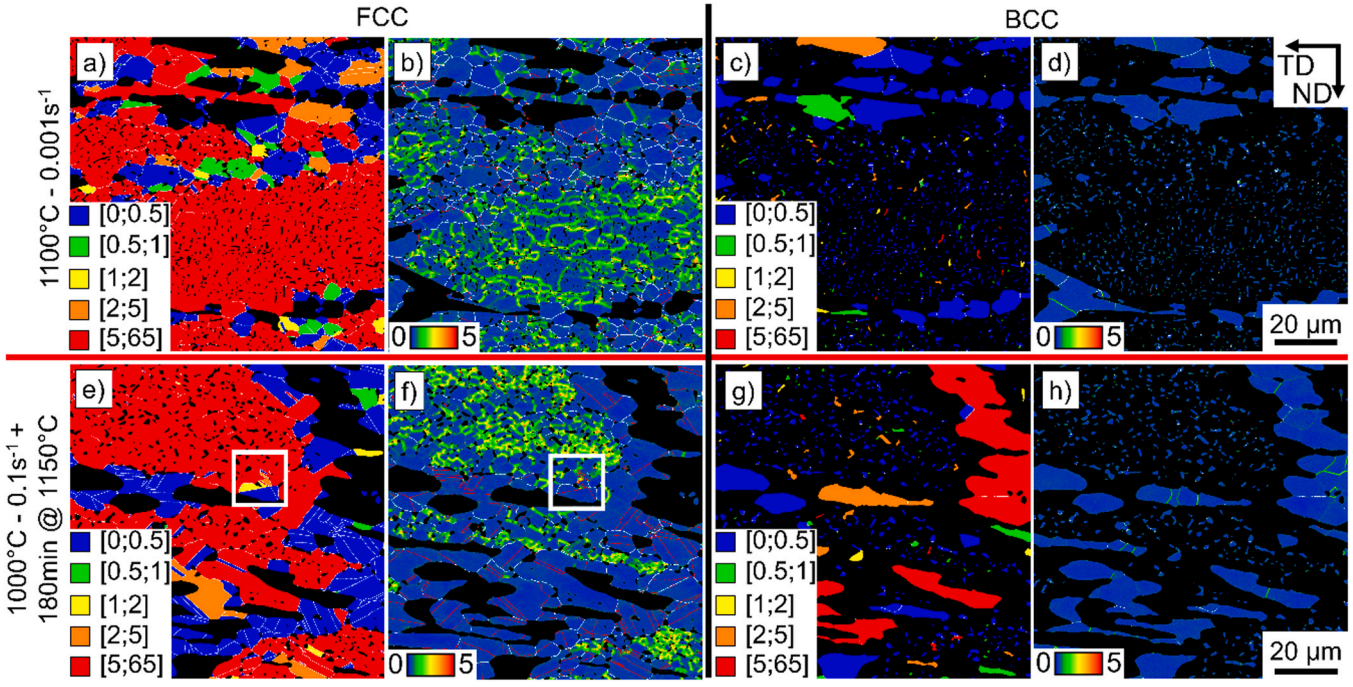

Fig. 14. EBSD results of the alloy deformed at a-d) 1100 °C and 0.001 s^{-1}; e-h) 1000 °C and 0.1 s^{-1} followed by annealing at 1150 °C for 180 min; showing the a,c,e,g) grain orientation spread (GOS) maps; b,d,f,h) KAM maps; for the a,b,e,f) FCC phase; c,d,g,h) BCC phase. The white lines indicate the HAGBs. The red lines in the KAM maps indicate the Σ3 boundaries. The white box in e,f) are shown in detail in Fig. 15.

secondary phase promote local lattice rotation and pin the grain boundaries of the FCC matrix. During plastic deformation, the eutectic BCC phase and secondary phase can act as a source for dislocation multiplication. Since they pin the HAGB movement by Zener pinning, they consequently retard dynamic, post-dynamic and static recrystallisation.

The eutectic BCC phase reinforces the FCC matrix. Therefore, its size and geometric configuration determine the load transfer between the eutectic BCC phase and the FCC matrix. The reinforcement by load transfer is maximum in an interconnected network of the eutectic BCC phase. As the material deforms, the eutectic BCC network bends due to plastic deformation, producing dislocations

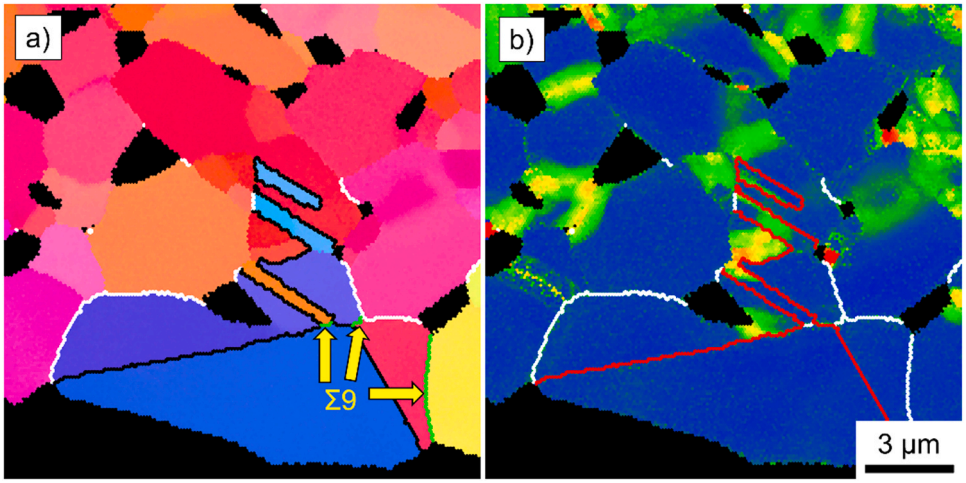

Fig. 15. EBSD results of the area indicated by the white box in Fig. 14(e,f) for the alloy deformed at 1000 °C and 0.1 s^{-1} followed by annealing at 1150 °C for 180 min; showing the a) inverse pole figure map; b) KAM map. The white lines indicate the HAGBs. The black lines in a) and the red ones in b) indicate the Σ3 boundaries. The green lines in a) indicate the Σ9 boundaries.

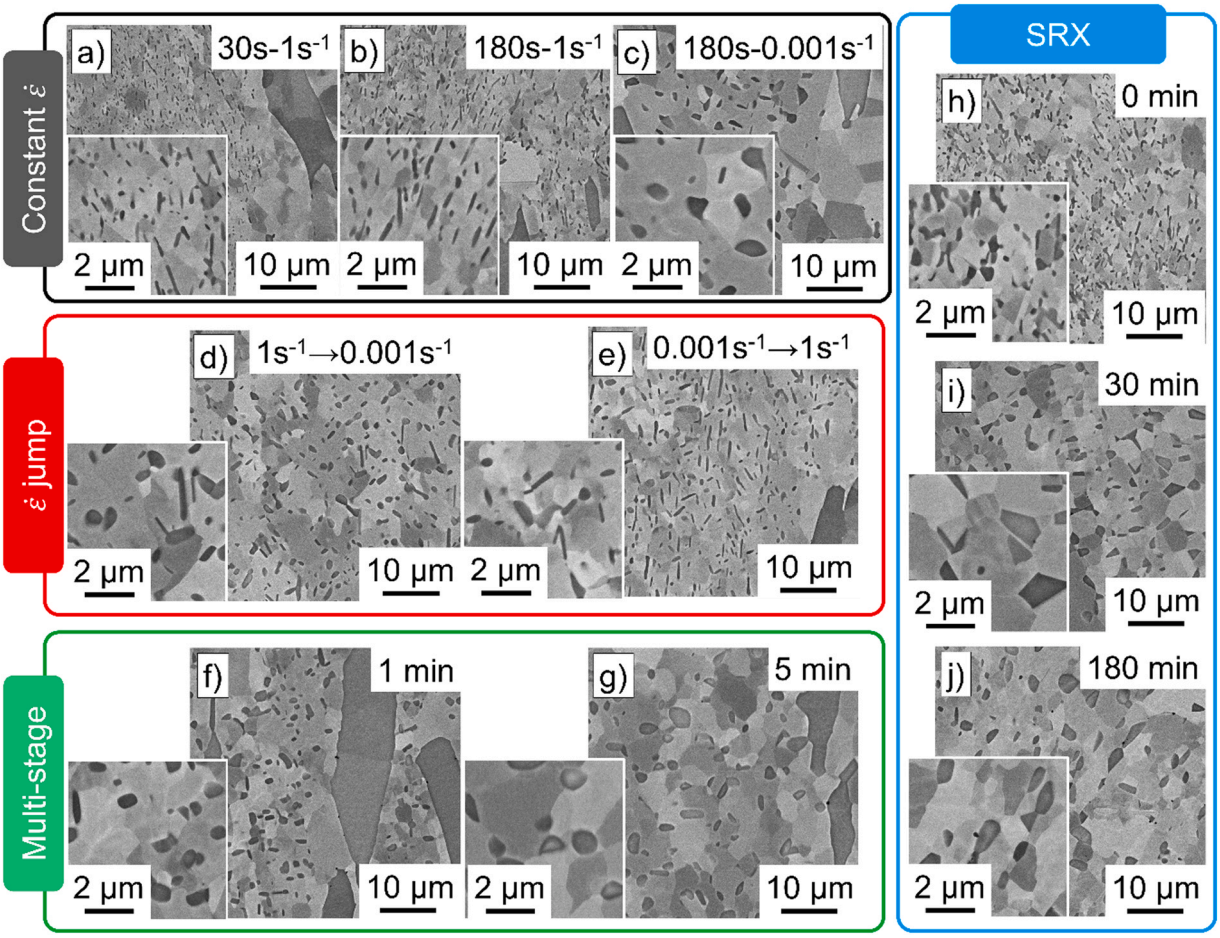

Fig. 16. Scanning electron micrographs (BSE mode) of the samples deformed at a-c) constant strain rate at 1100 °C; d,e) with strain rate jump at 1100 °C; f,g) with multi-stage deformation at 1100 °C; h-j) 1000 °C and 0.1 s^{-1} followed by annealing.

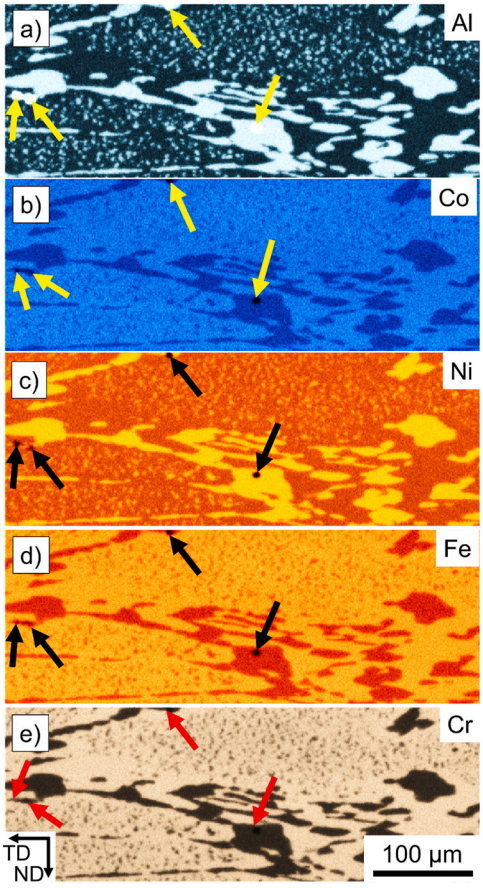

Fig. 17. Energy dispersive X-ray spectroscopy (EDX) maps of the deformed alloy at 1100 °C and 0.001 s^{-1} for the a) Aluminium; b) Cobalt; c) Nickel; d) Iron; e) Chromium. The arrows indicate the oxide inclusions.

within the eutectic BCC structure and a pronounced work hardening, as observed in the flow curves. The second stage of work hardening is associated with the intense multiplication of dislocations within the FCC phase due to interactions with the secondary phase, as observed in Fig. 2 for the tests carried at 1100 °C after 3 min

5. Summary and conclusions

A dual-phase cast high entropy alloy was produced by induction-melting. The alloy has a hypo-eutectic microstructure. A semi-continuous eutectic network of platelet-shape phases indexed for the EBSD measurements according to the BCC structure is embedded in a matrix of a phase indexed for the EBSD measurements according to the FCC structure. The eutectic BCC phase is enriched in Al and Ni. Secondary phase is formed during soaking if temperature and time is sufficiently long. They are also indexed for the EBSD measurements according to the BCC structure. Different thermomechanical treatments were carried out to determine the mechanisms of microstructural modification. The results allow the following conclusions to be drawn:

- Hot compression forms a fine and intricate substructure within the FCC matrix. However, the recrystallisation is limited and attributed to the pinning caused by the secondary phase that precipitate at high temperatures.
- Both dynamic and static recrystallisation occurs via nucleation and growth of new grains, forming Σ3 boundaries. In addition, the secondary phase that precipitate at high temperatures appear to rotate, accelerating the dynamic recovery by promoting lattice rotation within the FCC matrix, forming LAGBs and new HAGBs.
- Hot compression forms boundaries within the eutectic BCC phase, progressively increasing misorientation via CDRX. It is followed by a fragmentation of the semi-continuous network of the eutectic BCC phase, forming globular-like BCC particles.
- Flow softening occurs during hot compression due to a) a complex interaction of the dislocation rearrangement within the FCC phase and b) the fragmentation of the eutectic BCC phase.
- The strain rate jump tests show that the alloy accommodates the plastic deformation through microstructural changes, mainly considering the last deformation step.
- The multi-stage tests show that after the first step of deformation, the stress relaxes rapidly, and the relaxation continues for longer relaxation times at higher strains. The progressive fragmentation of the eutectic BCC phase and the progressive rearrangement of dislocations within the FCC substructure explain the lower stress values reached after relaxation for higher strains.
- Higher strains and/or longer annealing times are required to effectively refine the FCC microstructure.

CRediT authorship contribution statement

Conceptualization: **Ricardo Henrique Buzolin, Markus Masswohl, Franz Miller Branco Ferraz, Konrad Chrzan, Tomasz Dudziak, Maria Cecilia Poletti**; Methodology: **Ricardo Henrique Buzolin, Markus Masswohl, Franz Miller Branco Ferraz, Konrad Chrzan**; Formal analysis: **Ricardo Henrique Buzolin**; Investigation: **Ricardo Henrique Buzolin, Markus Masswohl, Franz Miller Branco Ferraz, Konrad Chrzan**; Resources: **Tomasz Dudziak, Maria Cecilia Poletti**; Writing – original draft: **Ricardo Henrique Buzolin, Franz Miller Branco Ferraz**; Writing – review & editing: **Ricardo Henrique Buzolin, Markus Masswohl, Franz Miller Branco Ferraz, Konrad Chrzan, Tomasz Dudziak, Maria Cecilia Poletti**; Visualization: **Ricardo Henrique Buzolin, Markus Masswohl**.

Data availability

The data will be available upon request to the corresponding author.

Declaration of Competing Interest

The authors declare that they have no known competing financial interests or personal relationships that could have appeared to influence the work reported in this paper.

Acknowledgements

The authors carried out this work under the following projects: KMM-VIN research fellowship from the European Virtual Institute on Knowledge-based Multifunctional Materials AISBL (KMM-VIN), and D-1303000107/CD-Laboratory for Design of High-Performance Alloys by Thermomechanical Processing with the support of the Christian Doppler Forschungsgesellschaft. Open access funding by the Graz University of Technology is also acknowledged.

References

[1] D.B. Miracle, O.N. Senkov, A critical review of high entropy alloys and related concepts, Acta Mater. 122 (2017) 448–511, https://doi.org/10.1016/j.actamat.2016.08.081
[2] E.P. George, D. Raabe, R.O. Ritchie, High-entropy alloys, Nat. Rev. Mater. 4 (8) (2019) 515–534, https://doi.org/10.1038/s41578-019-0121-4
[3] M.-H. Tsai, J.-W. Yeh, High-entropy alloys: a critical review, Mater. Res. Lett. 2 (3) (2014) 107–123, https://doi.org/10.1080/21663831.2014.912690

[4] Y.F. Ye, Q. Wang, J. Lu, C.T. Liu, Y. Yang, High-entropy alloy: challenges and prospects, Mater. Today 19 (6) (2016) 349–362, https://doi.org/10.1016/j.mattod.2015.11.026

[5] J. Chen, et al., A review on fundamental of high entropy alloys with promising high–temperature properties, J. Alloy. Compd. 760 (2018) 15–30, https://doi.org/10.1016/j.jallcom.2018.05.067

[6] S. Huang, et al., Mechanism of magnetic transition in FeCrCoNi-based high entropy alloys, Mater. Des. 103 (2016) 71–74, https://doi.org/10.1016/j.matdes.2016.04.053

[7] H.Y. Diao, R. Feng, K.A. Dahmen, P.K. Liaw, Fundamental deformation behavior in high-entropy alloys: an overview, Curr. Opin. Solid State Mater. Sci. 21 (5) (2017) 252–266, https://doi.org/10.1016/j.cossms.2017.08.003

[8] Z. Li, K.G. Pradeep, Y. Deng, D. Raabe, C.C. Tasan, Metastable high-entropy dual-phase alloys overcome the strength–ductility trade-off, Nature 534 (7606) (2016) 227–230, https://doi.org/10.1038/nature17981

[9] D. Li, Y. Zhang, The ultrahigh charpy impact toughness of forged AlxCoCrFeNi high entropy alloys at room and cryogenic temperatures, Intermetallics 70 (2016) 24–28, https://doi.org/10.1016/j.intermet.2015.11.002

[10] Y. Qiu, S. Thomas, M.A. Gibson, H.L. Fraser, N. Birbilis, Corrosion of high entropy alloys, npj Mater. Degrad. 1 (1) (2017) 15, https://doi.org/10.1038/s41529-017-0009-y

[11] G. Zhu, Y. Liu, J. Ye, Early high-temperature oxidation behavior of Ti(C,N)-based cermets with multi-component AlCoCrFeNi high-entropy alloy binder, Int. J. Refract. Met. Hard Mater. 44 (2014) 35–41, https://doi.org/10.1016/j.ijrmhm.2014.01.005

[12] J. Joseph, N. Haghdadi, K. Shamlaye, P. Hodgson, M. Barnett, D. Fabijanic, The sliding wear behaviour of CoCrFeMnNi and AlxCoCrFeNi high entropy alloys at elevated temperatures, Wear 428–429 (2019) 32–44, https://doi.org/10.1016/j.wear.2019.03.002

[13] N. Haghdadi, T. Guo, A. Ghaderi, P.D. Hodgson, M.R. Barnett, D.M. Fabijanic, The scratch behaviour of AlXCoCrFeNi (x=0.3 and 1.0) high entropy alloys, Wear 428–429 (2019) 293–301, https://doi.org/10.1016/j.wear.2019.03.026

[14] A.J. Zaddach, C. Niu, C.C. Koch, D.L. Irving, Mechanical properties and stacking fault energies of NiFeCrCoMn high-entropy alloy, JOM 65 (12) (2013) 1780–1789, https://doi.org/10.1007/s11837-013-0771-4

[15] S. Qiu, et al., Influence of lattice distortion on stacking fault energies of CoCrFeNi and Al-CoCrFeNi high entropy alloys, J. Alloy. Compd. 846 (2020) 156321, https://doi.org/10.1016/j.jallcom.2020.156321

[16] N.L. Okamoto, et al., Size effect, critical resolved shear stress, stacking fault energy, and solid solution strengthening in the CrMnFeCoNi high-entropy alloy, Sci. Rep. 6 (1) (2016) 35863, https://doi.org/10.1038/srep35863

[17] S. Huang, et al., Temperature dependent stacking fault energy of FeCrCoNiMn high entropy alloy, Scr. Mater. 108 (2015) 44–47, https://doi.org/10.1016/j.scriptamat.2015.05.041

[18] Y. Bin Kang, S.H. Shim, K.H. Lee, S.I. Hong, Dislocation creep behavior of CoCrFeMnNi high entropy alloy at intermediate temperatures, Mater. Res. Lett. 6 (12) (2018) 689–695, https://doi.org/10.1080/21663831.2018.1543731

[19] J.Y. He, et al., A precipitation-hardened high-entropy alloy with outstanding tensile properties, Acta Mater. 102 (2016) 187–196, https://doi.org/10.1016/j.actamat.2015.08.076

[20] Z.G. Wang, et al., Effect of coherent L12 nanoprecipitates on the tensile behavior of a fcc-based high-entropy alloy, Mater. Sci. Eng. A 696 (2017) 503–510, https://doi.org/10.1016/j.msea.2017.04.111

[21] T.-K. Tsao, A.-C. Yeh, H. Murakami, The microstructure stability of precipitation strengthened medium to high entropy superalloys, Metall. Mater. Trans. A 48 (5) (2017) 2435–2442, https://doi.org/10.1007/s11661-017-4037-6

[22] C.-J. Tong, et al., Mechanical performance of the AlxCoCrCuFeNi high-entropy alloy system with multiprincipal elements, Metall. Mater. Trans. A 36 (5) (2005) 1263–1271, https://doi.org/10.1007/s11661-005-0218-9

[23] Y.-F. Kao, T.-J. Chen, S.-K. Chen, J.-W. Yeh, Microstructure and mechanical property of as-cast, -homogenized, and -deformed AlxCoCrFeNi (0≤x≤2) high-entropy alloys, J. Alloy. Compd. 488 (1) (2009) 57–64, https://doi.org/10.1016/j.jallcom.2009.08.090

[24] B. Gwalani, et al., Stability of ordered L12 and B2 precipitates in face centered cubic based high entropy alloys - Al0.3CoFeCrNi and Al0.3CuFeCrNi2, Scr. Mater. 123 (2016) 130–134, https://doi.org/10.1016/j.scriptamat.2016.06.019

[25] D. Choudhuri, et al., Formation of a Huesler-like L21 phase in a CoCrCuFeNiAlTi high-entropy alloy, Scr. Mater. 100 (2015) 36–39, https://doi.org/10.1016/j.scriptamat.2014.12.006

[26] N. Haghdadi, S. Primig, M. Annasamy, P. Cizek, P.D. Hodgson, D.M. Fabijanic, Dynamic recrystallization in AlXCoCrFeNi duplex high entropy alloys, J. Alloy. Compd. 830 (2020) 154720, https://doi.org/10.1016/j.jallcom.2020.154720

[27] A. Korner, H.P. Karnthaler, C. Hitzenberger, Transmission electron microscopy study of cross-slip and of Kear-Wilsdorf locks in L12 ordered Ni3Fe, Philos. Mag. A 56 (1) (1987) 73–88, https://doi.org/10.1080/01418618708204467

[28] H.M. Daoud, A.M. Manzoni, N. Wanderka, U. Glatzel, High-temperature tensile strength of Al10Co25Cr8Fe15Ni36Ti6 compositionally complex alloy (high-entropy alloy, JOM 67 (10) (2015) 2271–2277, https://doi.org/10.1007/s11837-015-1484-7

[29] Z. Savaedi, R. Motallebi, H. Mirzadeh, A review of hot deformation behavior and constitutive models to predict flow stress of high-entropy alloys, J. Alloy. Compd. 903 (2022) 163964, https://doi.org/10.1016/j.jallcom.2022.163964

[30] Y. Lu, et al., A promising new class of high-temperature alloys: eutectic high-entropy alloys, Sci. Rep. 4 (1) (2014) 6200, https://doi.org/10.1038/srep06200

[31] T. Bhattacharjee, et al., Effect of low temperature on tensile properties of AlCoCrFeNi2.1 eutectic high entropy alloy, Mater. Chem. Phys. 210 (2018) 207–212, https://doi.org/10.1016/j.matchemphys.2017.06.023

[32] P. Shi, et al., Enhanced strength–ductility synergy in ultrafine-grained eutectic high-entropy alloys by inheriting microstructural lamellae, Nat. Commun. 10 (1) (2019) 489, https://doi.org/10.1038/s41467-019-08460-2

[33] M.H. Asoushe, et al., Thermal stability, microstructure and texture evolution of thermomechanical processed AlCoCrFeNi2.1 eutectic high entropy alloy, Mater. Sci. Eng. A 799 (2021) 140012, https://doi.org/10.1016/j.msea.2020.140012

[34] Z. Liu, Z. Xiong, K. Chen, X. Cheng, Large-size high-strength and high-ductility AlCoCrFeNi2.1 eutectic high-entropy alloy produced by hot-rolling and subsequent aging, Mater. Lett. 315 (2022) 131933, https://doi.org/10.1016/j.matlet.2022.131933

[35] Y. Zhang, X. Wang, J. Li, Y. Huang, Y. Lu, X. Sun, Deformation mechanism during high-temperature tensile test in an eutectic high-entropy alloy AlCoCrFeNi2.1, Mater. Sci. Eng. A 724 (2018) 148–155, https://doi.org/10.1016/j.msea.2018.03.078

[36] J. Charkhchian, et al., On the short-time thermal phase-stability of as-cast AlCoCrFeNi2.1 eutectic high entropy alloy, J. Mater. Res. Technol. 20 (2022) 551–560, https://doi.org/10.1016/j.jmrt.2022.07.058

[37] M.R. Rahul, S. Samal, S. Venugopal, G. Phanikumar, Experimental and finite element simulation studies on hot deformation behaviour of AlCoCrFeNi2.1 eutectic high entropy alloy, J. Alloy. Compd. 749 (2018) 1115–1127, https://doi.org/10.1016/j.jallcom.2018.03.262

[38] J. Jiang, M. Huang, Y. Wang, G. Xiao, Y. Liu, Y. Zhang, Unique hot deformation behavior and microstructure evolution of a dual FCC-phase CoCrCu1.2FeNi high entropy alloy, J. Alloy. Compd. 876 (2021) 160102, https://doi.org/10.1016/j.jallcom.2021.160102

[39] M. Annasamy, N. Haghdadi, A. Taylor, P. Hodgson, D. Fabijanic, Dynamic recrystallization behaviour of AlxCoCrFeNi high entropy alloys during high-temperature plane strain compression, Mater. Sci. Eng. A 745 (2019) 90–106, https://doi.org/10.1016/j.msea.2018.12.102

[40] H.T. Jeong, H.K. Park, W.J. Kim, Hot deformation behavior and processing map of a Sn0.5CoCrFeMnNi high entropy alloy with dual phases, Mater. Sci. Eng. A 801 (2021) 140394, https://doi.org/10.1016/j.msea.2020.140394

[41] H.T. Jeong, H.K. Park, W.J. Kim, Dynamic recrystallization and hot deformation mechanisms of a eutectic Al0.7CoCrFeMnNi high-entropy alloy, J. Alloy. Compd. 871 (2021) 159488, https://doi.org/10.1016/j.jallcom.2021.159488

[42] Q. Wang, et al., Hot compression behaviors and microstructure evolutions of a cast dual-phase NiCoFeCrAl0.7 high-entropy alloy, Intermetallics 138 (2021) 107314, https://doi.org/10.1016/j.intermet.2021.107314

[43] T. Cao, et al., High temperature deformation behavior of dual-phase Al0.6CoCrFeNi high-entropy alloys, J. Alloy. Compd. 836 (2020) 155305, https://doi.org/10.1016/j.jallcom.2020.155305

[44] I.S. Wani, G.D. Sathiaraj, M.Z. Ahmed, S.R. Reddy, P.P. Bhattacharjee, Evolution of microstructure and texture during thermo-mechanical processing of a two phase Al0.5CoCrFeMnNi high entropy alloy, Mater. Charact. 118 (2016) 417–424, https://doi.org/10.1016/j.matchar.2016.06.021

[45] W.J. Kim, H.T. Jeong, H.K. Park, K. Park, T.W. Na, E. Choi, The effect of Al to high-temperature deformation mechanisms and processing maps of Al0.5CoCrFeMnNi high entropy alloy, J. Alloy. Compd. 802 (2019) 152–165, https://doi.org/10.1016/j.jallcom.2019.06.099

[46] A. Nassar, A. Mullis, R. Cochrane, Z. Aslam, S. Micklethwaite, L. Cao, Rapid solidification of AlCoCrFeNi2.1 High-entropy Alloy, J. Alloy. Compd. 900 (2022) 163350, https://doi.org/10.1016/j.jallcom.2021.163350

[47] I.S. Wani, T. Bhattacharjee, S. Sheikh, P.P. Bhattacharjee, S. Guo, N. Tsuji, Tailoring nanostructures and mechanical properties of AlCoCrFeNi2.1 eutectic high entropy alloy using thermo-mechanical processing, Mater. Sci. Eng. A 675 (2016) 99–109, https://doi.org/10.1016/j.msea.2016.08.048

[48] K.-Y. Tsai, M.-H. Tsai, J.-W. Yeh, Sluggish diffusion in Co–Cr–Fe–Mn–Ni high-entropy alloys, Acta Mater. 61 (13) (2013) 4887–4897, https://doi.org/10.1016/j.actamat.2013.04.058

[49] J. Dąbrowa, et al., Demystifying the sluggish diffusion effect in high entropy alloys, J. Alloy. Compd. 783 (2019) 193–207, https://doi.org/10.1016/j.jallcom.2018.12.300

[50] G. Laplanche, P. Gadaud, O. Horst, F. Otto, G. Eggeler, E.P. George, Temperature dependencies of the elastic moduli and thermal expansion coefficient of an equiatomic, single-phase CoCrFeMnNi high-entropy alloy, J. Alloy. Compd. 623 (2015) 348–353, https://doi.org/10.1016/j.jallcom.2014.11.061